Theoretical modeling of ion mobility in superfluid ^{4}He

Steven L. Fiedler,[1] David Mateo,[2] Tatevik Aleksanyan,[3] and Jussi Eloranta[3,*]

[1]*Interdisciplinary Research Institute for the Sciences (IRIS) and the Department of Mathematics, California State University at Northridge, 18111 Nordhoff Street, Northridge, California 91330, USA*

[2]*Departament ECM, Facultat de Física, and IN2UB, Universitat de Barcelona, Diagonal 647, 08028 Barcelona, Spain*

[3]*Department of Chemistry and Biochemistry, California State University at Northridge, 18111 Nordhoff Street, Northridge, California 91330, USA*

(Received 30 August 2012; published 19 October 2012)

A method for calculating hydrodynamic added mass within the framework of time-dependent bosonic density functional theory (DFT) for superfluid ^{4}He is developed. As a calibration of the model, it is shown to reproduce the classical hydrodynamic limit for purely repulsive interactions. To model real systems for which experimental data are available, the following ions were considered: Be^+, K^+, Ca^+, Sr^+, and Ba^+ cations as well as the F^-, Cl^-, I^-, and Br^- anions. The DFT model requires the ion-helium pair potential data as input, which were obtained from electron structure calculations by employing coupled clusters theory. The resultant static liquid density profiles as calculated by DFT were found to be in good agreement with previously published quantum Monte Carlo data. The calculated added masses for the positive ions correlated directly with the experimentally observed ion mobility data, by which the ions could be separated into two different categories based on the degree of the first solvent shell following the ion. The calculated added masses for the negative ions were found to be in disagreement with the existing experimental data, suggesting the possibility that other negatively charged species were observed in previous experiments. The negatively charged ions are predicted to have mobilities (μ) within the range 0.8–1.0 cm^2 V^{-1} s^{-1} in superfluid helium at 1.3 K with the order $\mu(I^-) > \mu(Br^-) > \mu(Cl^-) > \mu(F^-)$.

DOI: 10.1103/PhysRevB.86.144522 PACS number(s): 67.25.D−, 67.90.+z

I. INTRODUCTION

Characterization of ion mobilities in bulk superfluid helium has been a subject of numerous experimental studies where an external electric field is employed to drift the ions through the liquid, resulting in a time-of-flight spectrum for the species.[1–4] The simplest of such ions is an electron, which forms a relatively large solvation cavity size (bubble radius $R_b \approx 18.5$ Å) that can be attributed to the repulsive nature of the electron-helium interaction and the large zero-point spread of the electron due to its light mass.[5,6] Due to this large volume occupied, electrons exhibit a relatively low ion mobility in the bulk (0.54 cm^2 V^{-1} s^{-1} at $T = 1.3$ K).[7] Indeed, most positive ions at this temperature, such as He_n^+ (0.88 cm^2 V^{-1} s^{-1}),[7] K^+ (0.85 cm^2 V^{-1} s^{-1}),[2,4] Rb^+ (0.78 cm^2 V^{-1} s^{-1}),[2] Cs^+ (0.78 cm^2 V^{-1} s^{-1}),[2] Be^+ (0.81 cm^2 V^{-1} s^{-1}),[8] Ca^+ (0.98 cm^2 V^{-1} s^{-1}),[2] Sr^+ (1.01 cm^{2}V^{-1}s^{-1}),[2] and Ba^+ (1.12 cm^{2}V^{-1}s^{-1}),[2] possess a higher mobility than the electron, indicating that they have a smaller effective mass in the liquid. Due to the relatively attractive interaction between the positive ions and helium, most cations are thought to form Atkins' "snowball" structures in the bulk, where the first solvent shells consist of rigid layers of helium with densities near or above that in the solid phase. Atkins' snowball model for K^+ predicts an effective ion mass 45× the mass of a helium atom and a radius of 6 Å.[9] Ion mobility in superfluid helium is essentially determined by the following aspects:[10] (i) the number of helium atoms dragged with the ion, (ii) dissipation of energy through emission of sound when the ion is accelerated in the liquid, (iii) roton emission when the Landau critical velocity is exceeded, (iv) vortex nucleation when the corresponding critical velocity is exceeded, and (v) interaction with thermal excitations when $T > 0$ K. The first effect is independent of the bubble radius (R_b) and does not depend strongly on temperature provided that the rigidly bound solvent atoms remain attached to the ion. The second effect depends on R_b through ion acceleration (phonon emission), and for an inviscid liquid it is given by $\frac{1}{2}V\rho_0$, where V is the bubble volume and ρ_0 is the bulk liquid density. In hydrodynamics, the combined effect of (i) and (ii) leads to the concept of added mass (m_{add}). The third and fourth processes depend on temperature, slightly, as the bulk dispersion relation changes somewhat as a function of temperature in the superfluid phase. The last process is strongly temperature-dependent as the thermal phonon and roton densities increase as a function of temperature. Note that at temperatures above ∼1 K, the ion-roton scattering process dominates over phonons. The scattering process is sensitive to the effective ion size in the liquid as the ion-roton scattering cross section is proportional to the ion radius squared. For example, a solvated electron in liquid helium predominantly exhibits repulsive behavior toward helium, and hence the contribution of the first effect (i.e., dragging of helium with it) to its overall mobility is vanishingly small. Furthermore, the typical velocities in the ion drift experiments were well below the superfluid critical velocity, which leaves the electron mobility to be mainly determined by roton-ion scattering and to a minor extent to the emission of sound. Based on the experimentally observed ion mobilities, the positively charged ion snowball structures appear to have smaller effective bubble radii than the electron.

Mobilities of negatively charged ions at 1.3 K, such as Cl^- (0.46 cm^2 V^{-1} s^{-1}),[1] F^- (0.47 cm^2 V^{-1} s^{-1}),[1] I^- (0.45 cm^2 V^{-1} s^{-1}),[1] Ba^- (0.41 cm^2 V^{-1} s^{-1}),[1] and Ga^- (0.41 cm^2 V^{-1} s^{-1}),[1] have been measured to have lower mobilities than the electron. Due to the negative charge, it is expected that the interaction between these ions and helium also exhibits

significant binding due to the charge-induced polarization interaction, and therefore they should form snowball structures similar to those of the positive ions discussed above. Thus the difference in mobilities between the positive and negative ions should be related to the difference in their solvation cavity size and the accompanying solvent shell structure (i.e., the overall effective ion size in the liquid). Previous theoretical investigations of the ion solvation structures in superfluid helium have relied on the well-known semiempirical bubble model[11–13] or more accurate quantum Monte Carlo (QMC) based methods,[14–18] whereas the low-temperature ion mobility has been discussed mostly in terms of the ion-roton collision model[3,19,20] or in terms of Stokes' law.[21,22] However, since the ion-roton collision cross section depends on the square of the ion radius in superfluid helium, the use of Stokes' law is not justified in this case.

In this study, we have carried out theoretical modeling of Cl^-, F^-, I^-, and Br^- anions as well as K^+, Be^+, Ca^+, Sr^+, and Ba^+ cations in superfluid helium by bosonic density functional theory (DFT). The main motivation is to develop a reliable theoretical model to estimate the ion mobilities and to investigate the origin of the experimentally observed difference between the positive and negative ion mobilities. The present calculations can be used to characterize the effective ion sizes based on the experimental mobility data. The paper is organized as follows: the employed DFT formalism is delineated, followed by relevant electron structure calculations of the pair potentials between the given ions and a ground-state helium atom. The validity of the applied DFT approach, which incorporates the ion-He pair potential, is validated against previous QMC results. Finally, mobilities of these ions are analyzed through time-dependent DFT calculations.

II. THEORY

The bosonic DFT model applied to describe superfluid ^{4}He and the corresponding numerical implementation have been described in detail previously.[23–25] All calculations included the kinetic energy correlation term present in the original Orsay-Trento (OT) functional as well as the solid helium penalty term.[26,27] The ground-state solution for the ion-liquid system was obtained by the imaginary-time propagation method. For both the imaginary- and real-time propagation, the applied time step ranged from 0.2 to 5 fs with a cylindrical spatial grid consisting of 4096 points along the z coordinate and 2048 points along the radial dimension. A fixed 0.1 Å step size was employed along both coordinates. The large grid was chosen in order to minimize possible boundary reflections of long-wavelength phonons created during the ion drift dynamics. Rather than performing an analytic calculation to eliminate the angular dependency from the OT functional with subsequent direct numerical integration for the remaining degrees of freedom,[28] we employed a mixed Fourier(along z)-Hankel(along r) transformation, which can be used to calculate the underlying convolution integrals with greater efficiently in two dimensions. Furthermore, only minimal changes to the existing three-dimensional (3D) numerical implementation of the OT functional are needed with this approach. Note that a full 3D calculation employing the grid size required in this study would need nearly 5 TB of memory, which clearly exceeds the capacity of modern supercomputers. In two dimensions, the same calculation requires only $\sim$1 GB of memory, which means that the calculations can be executed with very modest memory requirements. In addition, the 2D Fourier-Hankel transformation provided a significant improvement in efficiency as compared to its 3D equivalent. The terms containing dot products in the OT Hamiltoninan (i.e., the kinetic energy correlation and the backflow) can also be evaluated using this method by carrying out the integrations in cylindrical coordinates, while retaining the Cartesian form for the dot products. Both the 2D and 3D versions of OT have been implemented in the LIBDFT library and the underlying parallel grid library LIBGRID.[29,30] The bulk liquid calculations implemented the continuous liquid edge by a Neumann boundary condition, whereas the helium droplet calculations implied a Dirichlet boundary. During the imaginary-time iterations, the bulk density was maintained in the liquid at the simulation boundary by rescaling to the fixed bulk value and by conserving the number of He atoms during the iterations for the droplet calculations. The ion zero-point spread inside the bubble was not included in the model as the species considered are sufficiently heavy so that they are localized in the middle of the solvation cavity (estimated full width at half height <0.1 Å for the ion wave function). The ion drift in an external electric field directed along the z axis was included in the calculation through the additional potential term $V(z) = -qE_z \times z$, where q is the ion charge, E_z denotes the external electric field strength along the z axis (10^{-7} a.u.), and z is the ion position z coordinate. Thus the ion movement occurs along the z axis, whereas only sound propagation may occur along the radial direction. The classical degrees of freedom for the ion were propagated by using the velocity Verlet algorithm[31] alongside the time-dependent DFT equation for the liquid. These two equations were included in a predict-correct scheme to improve the numerical stability of the method.

At $T = 0$ K, the number of helium atoms dragged with the ion as well as dissipation of energy due to phonon emission can be calculated from the instantaneous added mass (in units of He atoms and excluding the ion mass):

$$m_{\mathrm{add}}(t) = \left(\frac{E_z}{F_{\mathrm{tot},z}(t)} - 1\right)\frac{m_{\mathrm{ion}}}{m_{\mathrm{He}}}, \tag{1}$$

where $F_{\mathrm{tot},z}$ is the total force acting on the ion (i.e., combined external electric field and liquid response) and m_{ion} and m_{He} are the ion and helium masses, respectively. The total force acting on the ion is given by

$$\begin{aligned} F_{\mathrm{tot},z}(t) &= E_z - \frac{\partial}{\partial z}\int V_{\text{ion-He}}(|r-r'|)\rho(r',t)d^3r' \\ &= E_z - \int\left(\frac{\partial}{\partial z}V_{\text{ion-He}}(|r-r'|)\right)\rho(r',t)d^3r', \end{aligned} \tag{2}$$

where $r = (x,y,z)$, $r' = (x',y',z')$, $V_{\text{ion-He}}$ is the ion-helium pair potential, and ρ denotes the time-dependent liquid density. To achieve numerically stable results, the derivative appearing on the right-hand side of Eq. (2) was evaluated analytically and the resulting function was then mapped on a spatial grid by using linear interpolation. To further improve the stability,

the integral form of Eq. (1) was used (in units of m_{He}):

$$m_{\mathrm{add}}(t) = \left(\frac{2E_z \Delta z(t)}{m_{\mathrm{ion}} v_z^2(t)} - 1\right) \frac{m_{\mathrm{ion}}}{m_{\mathrm{He}}}, \tag{3}$$

where Δz is the ion displacement along the z axis and v_z is the z component of the ion velocity. The added mass can be related to the hydrodynamic radius R_b through (assuming a spherical object)

$$m_{\mathrm{add}} = m_{\mathrm{He}} \int_0^{R_b} \tilde{\rho}(r) d^3 r, \tag{4}$$

$$\tilde{\rho}(r) = \begin{cases} [\rho_0 - \rho(r)]/2 + \rho(r) & \text{when } \rho(r) < \rho_0, \\ \rho(r) & \text{when } \rho(r) \geqslant \rho_0, \end{cases} \tag{5}$$

where R_b represents an effective ion radius, which accounts for the movement of displaced liquid by the ion [the first line in Eq. (5)] and the dragging of liquid with the ion [the second line in Eq. (5)]. For a spherical object with no binding and a Heaviside liquid density profile, this reduces to the familiar expression from hydrodynamics:

$$m_{\mathrm{add}} = \frac{1}{2} V \rho_0 = \frac{2\pi}{3} R_b^3 \rho_0. \tag{6}$$

The key observable in the experiments is the ion mobility μ, which is defined as the ratio between the observed ion velocity (v_{ion}) and the applied external electric field strength (E_z):

$$\mu = \frac{v_{\mathrm{ion}}}{E_z}. \tag{7}$$

In the limit of zero temperature, the mobility can be obtained from time-dependent DFT calculations by observing the long-time limit for the added mass [Eq. (3)]. Note that at 0 K, the ion terminal velocity is limited by phonon (sound) and eventually by roton/vortex (critical behavior) emission.

When $T > 1$ K, the present formulation of the time-dependent DFT cannot be used to directly obtain the reduction of ion mobility that occurs through thermal phonon/roton scattering. In this regime, the ion mobilities are usually taken to be proportional to the inverse of the ion-roton collision cross section squared: $\mu \propto (R_b + d)^{-2}$, where d corresponds to the effective roton (quasiparticle) radius. Since for electron bubbles $R_b \gg d$ [d corresponds approximately to the size of a single helium atom in the liquid; ~4 Å (Ref. 10)], the mobility is often taken to be proportional to just R_b^{-2}. However, for smaller ions, R_b and d may be comparable, and in this case d must be included in the estimate. Provided that the ion-roton cross sections follow this simple geometric proportionality, we can obtain relative ion mobilities:[3,10,32]

$$\frac{\mu_1}{\mu_2} = \frac{(R_{b,2} + d)^2}{(R_{b,1} + d)^2}, \tag{8}$$

where the indices 1 and 2 refer to the two different ions under consideration. Note that in the limit of Stokes' law, the relative mobility would just depend on the ratio between the two radii. In the temperature region of the relevant experiments ($T \geqslant 1.2$ K),[2] the mobilities are dominated by roton rather than phonon scattering, as the roton number density quickly outpaces phonons above 1 K and thus the mobilities are expected to be inversely proportional to R_b^2 rather than R_b as given by Stokes' formula.[33] However, previously the application of Stokes' formula has provided excellent agreement with the experimentally observed electron mobility data when used together with the semiempirical charge mobility model of Aitken *et al.*[21,22]

Previously, the spherical bubble radius R_b has been defined as the mass barycenter of the bubble interface:[34]

$$\int_0^{R_b} \rho(r) d^3 r = \int_{R_b}^{\infty} [\rho_0 - \rho(r)]\, d^3 r, \tag{9}$$

where ρ_0 corresponds to the bulk liquid density. It is apparent that this definition would fail when distinct solvation shells around the impurity are present (e.g., for charged ionic species). The formula based on the concept of added mass [i.e., Eq. (5)] is thus more general as it can account for the presence of bound solvent layers appropriately. However, as elaborated in the next section, the radius R_b appearing in Eq. (8) may not necessarily correspond to that used in Eqs. (4) and (5) due to the fact that the roton scattering process may be sensitive to the solvent shell structure far away from the ion.

By increasing the ion velocity from the typically accessed linear regime [i.e., where Eq. (7) holds], critical phenomena can be observed.[2] There are two possibilities for such behavior: (i) roton emission and (ii) vortex nucleation by the ion. At $T = 0$ K, the first process may act as a limiting factor dictating the terminal velocity for the ion, whereas the second is observed at high velocities (i.e., high external electric field strengths). Both phenomena can be modeled with time-dependent DFT simulations by determining the abrupt changes in the ion velocity versus its added mass, m_{add}. When a new dissipation channel becomes active, a sudden increase in m_{add} should occur.

III. RESULTS AND DISCUSSION

The ion-helium pair potentials were calculated by using the restricted coupled clusters theory with single, double, and perturbative connected triple excitations [CCSD(T)] as implemented in the MOLPRO code.[35,36] When this approach is employed together with a large augmented basis sets (e.g., aug-cc-pV5Z), it has been shown to typically produce a wave-number accuracy in the van der Waals region.[37,38] Smaller basis sets, such as those used here for K^+, Sr^+, and Ba^+, may have, as discussed later, a limited ability to fully recover the dispersion interaction with He atoms. All the calculated pair potentials were corrected for basis-set superposition error (BSSE) by the counterpoise correction method of Boys and Bernardi.[39] For most species [F (Refs. 40 and 41), Cl (Ref. 42), Br (Ref. 43), Ga (Ref. 43), and Be (Ref. 44)], an augmented correlation consistent basis set aug-cc-pV5Z (AV5Z) was applied, whereas cc-pV5Z (V5Z) was used for Ca and Ga, and a quadruple zeta level Def2-QZVPPD basis set was used for K^+,[45] Sr^+,[45] and Ba^+.[45] The Sr and Ba basis sets include the inner core electrons through the effective core potential approach, which reduces the number of electrons requiring explicit treatment of electron correlation. All ions considered in this study were spherically symmetric with the exception of Ga^-, which has a ^3P ground state. The two possible He atom approaches toward Ga^- produce Σ and Π molecular states, which were calculated separately as the standard CCSD(T) method can be applied to get the lowest root in each irreducible representation within

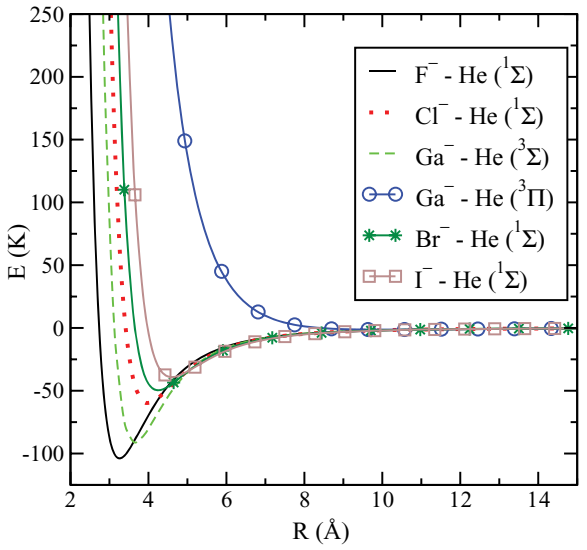

FIG. 1. (Color online) Calculated pair potentials for halogen anions interacting with a ground-state helium atom. Note that Ga^- is nonspherical as two possible electronic states (Σ and Π) arise from the outmost atomic s and p orbitals on He and Ga, respectively.

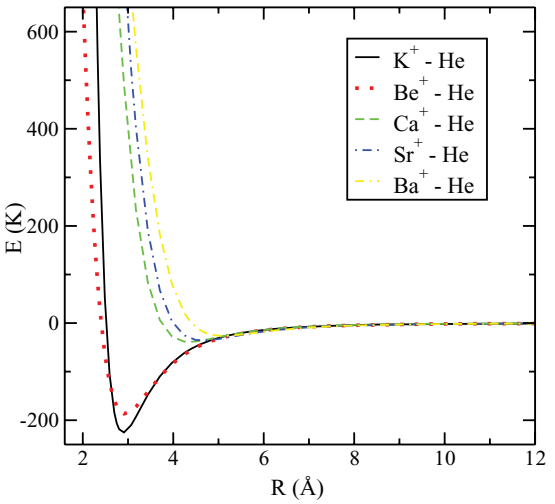

FIG. 2. (Color online) Calculated pair potentials for the cations K^+, Be^+, Ca^+, Sr^+, and Be^+ interacting with a ground-state helium atom.

a given point group (i.e., C_{2v}). To provide the pair potential data in a functional form, the calculated data were fitted to the following equation:

$$V(R) = A_0 e^{-A_1 R} - \frac{A_2}{R^4} - \frac{A_3}{R^6} - \frac{A_4}{R^8} - \frac{A_5}{R^{10}}, \qquad (10)$$

where A_0 through A_5 are constants for a given pair potential. Despite the fact that this equation bears the exact same form as is typically applied in describing atom-atom long-range interactions, it should be stressed that the parameters given here merely provide a way to parametrize the potential and that the individual values of the parameters should not be interpreted to have any physical significance (e.g., A_i are not to be interpreted as dispersion coefficients). The least-squares fitting process of the *ab initio* data to Eq. (10) is often plagued by the existence of local minima and problematic behavior high in the repulsive wall. The latter issue is typically evidenced as a rapid turnover of the function at short distances, after which it tends toward $-\infty$. For this reason, the pair potential parameter set must also specify the minimum distance where the potential is still valid on the repulsive wall ($R_{\min}$).

The calculated pair potential data for the anions and cations are shown in Figs. 1 and 2, respectively. A comparison of the current pair potentials with the previous literature values is

TABLE I. Overview of positive ion–He pair potentials: CCSD(T) denotes coupled clusters theory with single, double, and perturbative triples; CI denotes configuration interaction; Exp-repulsion+disp denotes exponential repulsive wall combined with dispersion series; HF+dispersion denotes Hartree-Fock for the repulsive wall combined with the standard dispersion series; MP4 denotes fourth-order Møller-Plesset perturbation theory. The basis sets are described according to the standard notation; for details, see the given reference. D_e and R_m denote the dissociation energy and the potential minimum, respectively.

Ion	Method	D_e (K)	R_m (Å)	Source
K^+	CCSD(T)/Def2-QZVPPD	225	2.9	Present work
	CCSD(T)/cVQZ	217	2.9	Present work
	CI	255	2.85	Ref. 48
	HF+dispersion	246	2.87	Ref. 49
	Exp-repulsion+disp	237	2.90	Ref. 47
	CI/Huzinaga	212	2.91	Ref. 46
Ca^+	CCSD(T)/V5Z	39	4.4	Present work
	CCSD(T)/Def2-QZVPPD	44	4.4	Present work
	CISD/See Ref.	42	4.4	Ref. 50
	Exp-repulsion+disp	73	4.1	Ref. 51
Be^+	CCSD(T)/AV5Z	187	2.9	Present work
	CCSD(T)/Def2-QZVPPD	157	3.0	Present work
	CCSD(T)/d-AV5Z	192	2.92	Ref. 52
	QCISD/Be:6-311++G(3df,3dp)/He:AVQZ	178	2.96	Ref. 53
	MP4/6-311G(2df/2pd)//MP2/6-31G**	100	3.13	Ref. 54
Sr^+	CCSD(T)/Def2-QZVPPD	36	4.6	Present work
Ba^+	CCSD(T)/Def2-QZVPPD	26	5.1	Present work

TABLE II. Overview of halogen ion–He pair potentials: CCSD(T) denotes coupled clusters theory with single, double, and perturbative triples; CI denotes configuration interaction; Exp-repulsion+disp denotes exponential repulsive wall combined with dispersion series. The basis sets are described according to the standard notation; for details, see the given reference. D_e and R_m denote the dissociation energy and the potential minimum, respectively.

Ion	Method	D_e (K)	R_m (Å)	Source
F^-	CCSD(T)/AV5Z	104	3.3	Present work
	CCSD(T)/AVQZ	108	3.25	Ref. 55
	CCSD(T)/AV5Z	107	3.26	Ref. 56
	CCSD(T)/VTZ + mid bond	106	3.27	Ref. 57
Cl^-	CCSD(T)/AV5Z	60	4.0	Present work
	CCSD(T)/AVQZ	60	4.0	Ref. 55
	CCSDT(T)/AVQZ	57	4.0	Ref. 58
	CI/Huzinaga	63	4.1	Ref. 46
	Exp-repulsion+disp	114	3.5	Ref. 47
Br^-	CCSD(T)/AV5Z	50	4.2	Present work
	CCSD(T)/AVQZ-PP	47	4.30	Ref. 55
	Exp-repulsion+disp	58	4.0	Ref. 47
I^-	CCSD(T)/AV5Z-PP	39	4.6	Present work
	CCSD(T)/AVQZ-PP	36.2	4.70	Ref. 55

summarized in Tables I and II and the potential parameters according to Eq. (10) are given in Table III. For the halogen anion-helium pair potentials, the well depths and the minima are in good agreement with the previously published results using a similar level of theory, i.e., generally within 5 K for energy at the potential minima and less than 0.1 Å for the position of the minima. For the cations, there is a larger variation between the current and the previously published data. For K^+-He, for example, the previous calculations have either relied on lower-level *ab initio* methods [e.g., the configuration interaction with single and double excitations method (CISD)] to obtain the van der Waals attraction (dispersion), or on the Hartree-Fock (HF) method to approximate the form of the repulsive wall combined with a dispersion series derived from experimental data.[46–49] Note that since the standard CISD method is not size-consistent, the counterpoise-type BSSE correction cannot be applied. Depending on the basis set employed, this can introduce significant inaccuracy into the pair potentials, which should ideally vanish in the limit of a complete basis set. Note that the CCSD(T) method applied in the present study is size-consistent, which allows BSSE correction. The above semiempirical technique, based on using HF repulsion and dispersion determined by experimental data, is not a straightforward approach for two reasons: (i) the dispersion coefficients must be known accurately based on the available experimental data, and (ii) there is a delicate balance between the HF-derived repulsive wall and the van der Waals interaction, which can amplify the error in the overall pair potential and especially near the van der Waals minimum. For the K^+-He interaction, we considered two different basis sets (Def2-QZVPPD and cVQZ; see Table I), which produced identical potential minima positions but the well depths differed by 8 K. For consistency, we employ the Def2-QZVPP basis results in this study as this basis set is also available for the heavier nuclei. However, it appears that this basis set underestimates the well depth by 15% for Be^+-He, and one would expect this level of accuracy to extend to the heavier ions as well. However, by comparing the performance of this basis set for Ca^+ against the unaugmented V5Z, it appears to provide a similar level of accuracy. Hence it is expected that the error would be less than the worst-case estimate of 15% based on Be^+-He. The nonspherical Ga^--He pair potential data are only given for reference, as they were not employed in the following DFT calculations.

The present form of the OT functional has been successfully applied earlier to describe the solvation of Be^+ as well as the liquid-solid phase transition.[26,27] To verify that it can be used to describe the solvation of the relatively strongly bound

TABLE III. Pair potential parameters for the ion-helium interaction (atomic units) according to the parametrization given in Eq. (10).

Ion	A_0	A_1	A_2	A_3	A_4	A_5	$R_{\min}$
Ca^+	4.83692	1.23684	0.273202	59.5463	1134.51	0.0	5.0
K^+	140.757	2.26202	0.722065	1.44039×10^{-3}	356.303	1358.98	4.0
Be^+	4.73292	1.53925	0.557845	26.7013	0.0	0.0	3.4
Sr^+	3.64975	1.13451	0.293483	99.0206	693.904	0.0	5.0
Ba^+	10.5807	1.24428	0.695007	31.9518	2087.89	0.0	7.3
Cl^-	11.1909	1.50971	0.721860	17.2434	0.0	0.0	4.2
F^-	5.16101	1.62798	0.773982	1.09722	0.0	0.0	4.1
I^-	13.6874	1.38037	0.696409	37.3331	0.0	0.0	4.1
Br^-	12.5686	1.45686	0.714525	24.1140	0.0	0.0	5.0

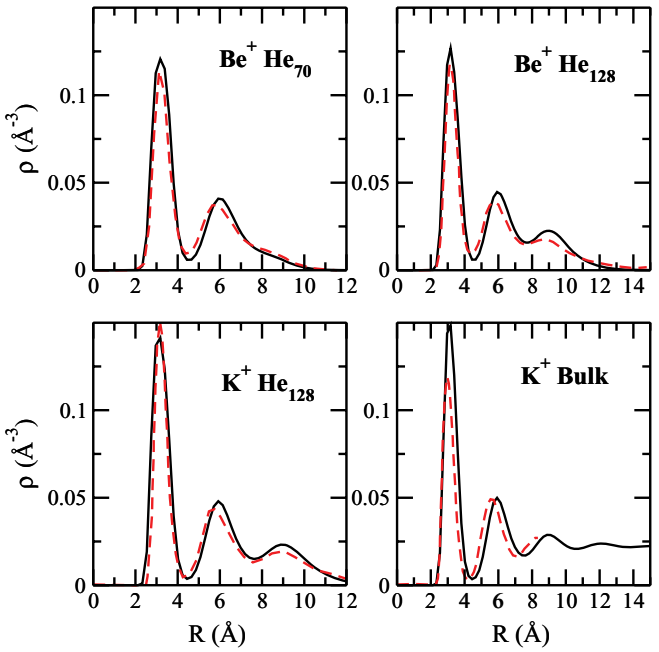

FIG. 3. (Color online) Comparison between the calculated liquid density profiles from DFT (continuous black line) and previous QMC calculations (dashed red line).[15,16,27]

ions, a comparison between QMC and the present OT-DFT calculations is given in Fig. 3 for K^+. The agreement is excellent for the helium droplets, whereas for the bulk, there is a noticeable difference in the first solvation shell, with OT-DFT predicting slightly higher density than QMC. This difference is rather surprising since the changes in the nearest solvent layers appear to saturate after ∼128 He atoms and, in this sense, it appears that there is even such a discrepancy between the two QMC methods used for the droplet and the bulk calculations. The static OT-DFT density profiles for the other cations considered are shown in Fig. 4. With the exception of Be^+, these ions are much less bound than K^+ and the variations in the liquid density are significantly less

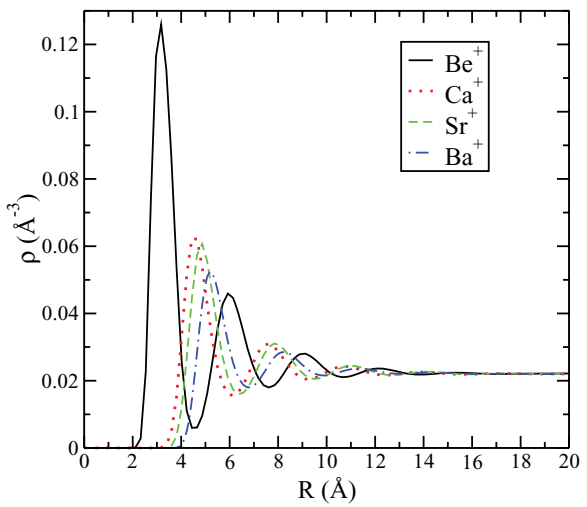

FIG. 4. (Color online) Calculated ground-state liquid densities as obtained from DFT calculations for Be^+, Ca^+, Sr^+, and Ba^+.

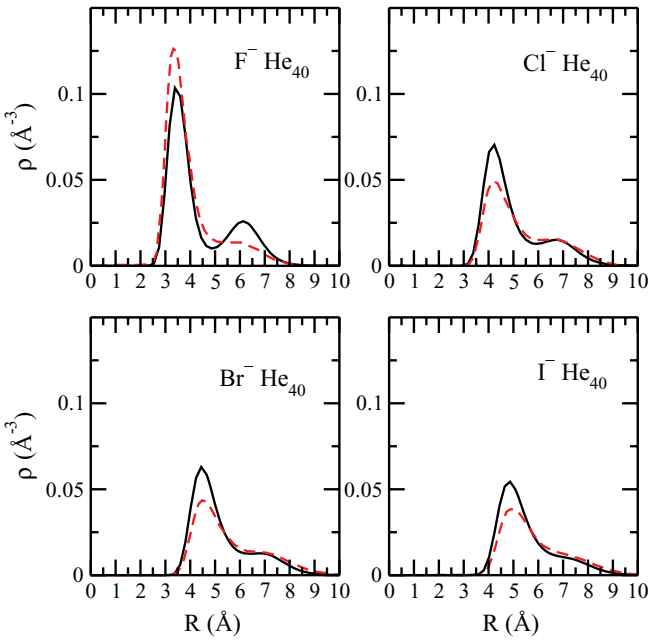

FIG. 5. (Color online) Comparison of the calculated liquid density profiles for halogen anions in helium clusters. The continuous black line corresponds to present DFT calculations and the dashed red line to previous QMC calculations.[55]

pronounced. The calculated density profiles for Be^+ and Ca^+ also compare favorably with respect to the first solvent shell structure obtained in previous QMC calculations for clusters with 70 He atoms.[14] As shown for the anions in Fig. 5, however, the comparison between the static density profiles obtained from OT-DFT and QMC is not as straightforward. For F^-, the QMC calculations predict a higher density in the first solvent shell as compared to OT-DFT, but the situation appears to be the opposite for the rest of the ions. For F^-, there is also a significant difference in the second solvation shell density. Unfortunately, the QMC data are only available for small He clusters, thus precluding a more detailed analysis. Based on the overview given in Table III, the observed difference cannot be explained in terms of different pair potentials being applied in the calculations, but the origin must lie between the applied theoretical approaches for describing superfluid helium.

To demonstrate the applicability of Eq. (3) in calculating the added mass within the DFT framework, a set of purely exponential spherical potentials (see Table IV) with varying radii was used. Note that for such exponentially repulsive

TABLE IV. Parameters for the exponentially repulsive potential, $A_0 \exp[-A_1(r + A_2)]$, along with the center of mass for the interface (R_b) and the calculated added mass (m_{add}).

A_0 (Hartree)	A_1 (Å)	A_2 (Å)	R_b (Å)	m_{add} (units of m_{He})
3.8003×10^5	1.6245	−4.2	12.0	86.5
3.8003×10^5	1.6245	−2.6	10.2	46.2
3.8003×10^5	1.6245	−1.6	9.0	28.6
3.8003×10^5	1.6245	0.0	7.1	11.8
3.8003×10^5	1.6245	1.6	5.3	3.6
3.8003×10^5	1.6245	2.1	4.8	2.2

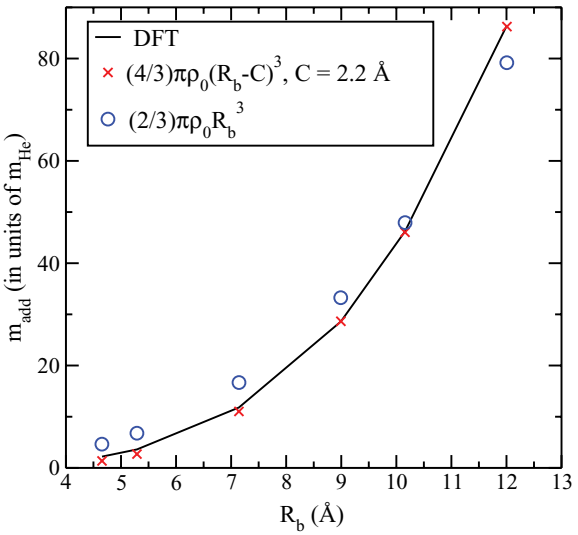

FIG. 6. (Color online) Comparison between the calculated effective mass using time-dependent DFT + Eq. (3) and the hydrodynamic formula of Eq. (6). Note that the DFT liquid density profiles have significant interfacial width and thus there is only an approximate relationship between the two models. For a discussion of the modified hydrodynamic formula, see the text.

potentials, there is no rigid solvent shell around the impurity and hence the added mass should be strictly related to the bubble volume. The calculated added mass is plotted in Fig. 6 as a function of the interface barycenter [R_b; Eq. (9)] along with the classical added mass [see Eq. (6)]. The results obtained from these two models correlate well. A perfect match was not expected, as the bubble structures from DFT exhibit a finite interface width. Peculiarly, the DFT calculations exactly match an expression that depends directly on the displaced liquid volume with an artificial shift of the interface barycenter to the region where the liquid density increases rapidly from zero [i.e., $R_b - C$, $C = 2.2$ Å; cf. Eq. (6)]. It is expected that the offset C depends on the interface width, and in the limit of a Heaviside profile, this constant should converge toward zero to recover the classical result.

Next, the actual ionic systems, which include the pronounced solvent layer structure, are considered. After an initial ion acceleration period (typically ∼3 ps) in the time-dependent DFT calculations, the calculated instantaneous ion added mass converges to approximately a constant value, which is then taken as m_{add}. However, we have observed that small amplitude periodic oscillations persist (typically $\pm 0.3 \times m_{\text{He}}$) even at long times, which appear to correspond to acceleration/deceleration events of the ion in the liquid. These in turn appear to be related to the ion dropping off and picking up small amounts of liquid as it travels in the superfluid. As in classical hydrodynamics, this leads to dissipation of energy through emission of sound. This process persists for several hundred picoseconds and therefore appears to be part of the actual long-time ion propagation dynamics. A summary of the calculated added masses using Eq. (3) is shown in Table V (averaged over the small-amplitude oscillations), along with the derived spherical bubble radii R_b obtained from Eqs. (4) and (5). The current DFT calculations reproduce the previous QMC derived added mass for K^+ (Ref. 15) with a very good accuracy considering that the two calculations did not even use exactly the same K^+-He pair potential. Note that Atkins' estimate of $R_b \approx 6$ Å for K^+ predicts that the second solvation shell would also follow the ion. For the other ions considered, the calculated added masses indicate either a complete following of the first full solvent shell (e.g., Be^+, K^+) or only a partial following of the first solvent shell for the less bound ions (e.g., Ca^+, Sr^+, Ba^+, and most of the halogen ions). In the current calculations, the ion velocities reach ∼1 m/s at maximum and therefore the dynamics is mostly sensitive to the phonon response of the liquid. For such small velocities, hydrodynamic approximations are also able to reproduce the correct ion added masses, provided that liquid density profiles are available that have been computed by some other method.[59] In the present case, however, DFT is used to calculate both the initial stationary liquid density profile as well as the time evolution in the presence of the external electric field, which allows the method to be used without any external data, and it can also be used for studying critical phenomena at higher electric fields.

TABLE V. Ion added masses as obtained from time-dependent DFT calculations using Eq. (3), the derived bubble radii according to Eqs. (4) and (5), and experimental mobilities μ at 1.3 K are shown.[1,2,4,7,8] Note that the added mass m_{add} excludes the ion mass and is given in units of m_{He}. The electron bubble radius and its added mass were approximated based on the previously published data,[5,10] and the QMC reference data for K^+ were taken from Ref. 15. The calculated values of R_b by using both Eq. (8) and Stokes' law are also shown for comparison (electron mobility and radius as the reference).

Ion	m_{add} (m_{add} QMC)	R_b (Å) [Eq. (5)]	R_b [Eq. (8)]	R_b (Stokes)	μ (cm^2 V^{-1} s^{-1})
Be^+	19.7	5.9	14.4	12.7	0.81
K^+	17.2 (17.4)	5.6	13.9	12.1	0.85
Sr^+	4.1	4.3	12.5	10.2	1.01
Ca^+	4.3	4.4	12.7	10.5	0.98
Ba^+	4.0	4.7	11.6	9.0	1.12
F^-	13.0	6.9	20.1	21.4	0.47
Cl^-	9.0	4.5	20.4	21.9	0.46
I^-	4.5	4.5	20.6	22.4	0.45
Br^-	4.8	4.3			
e^-	170	18.5			0.54

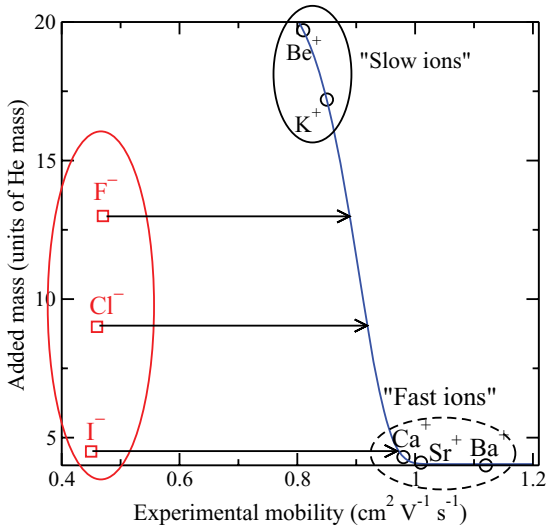

FIG. 7. (Color online) Relationship between calculated added mass and experimental ion mobility data. The positive ions can be divided into two categories: fast and slow ions. The halogen anions appear separate from the positive ion data, and their expected mobilities are indicated by arrows. The line connecting the positive ion mobility data is drawn as a guide to the eye.

Table V also includes estimates for R_b by using Eq. (8) and Stokes' law. Since Stokes' law should not be applicable in the present case, we concentrate on comparing the R_b derived from the added mass calculation with the R_b from the ion-roton scattering formula. It is clear that there is a significant difference between the two radii, approximately 8 Å. The radii derived using Eq. (8) appear to correlate with the position near the weak fourth through fifth solvent shells (cf. Fig. 4). The density oscillations in this region have very small amplitude, ∼2% from the bulk density, but these may still be sufficient to trigger roton scattering from the bubble. Based on this interpretation, it would then appear that the definitions given by Eqs. (4) and (5) and Eq. (8) correspond to different R_b, with the former related to the immediate first solvent shell location and the latter to the much weaker solvent layer structure farther away from the ion. This also means that there should not be an exact relationship between the added mass and the radius R_b derived from Eq. (8) because the added mass is not necessarily a direct measure of the solvent shell structure far away from the ion. However, a fairly good correlation between the ion added mass and the ion mobility can be obtained as demonstrated in Fig. 7 (the data point for the solvated electron is off the scale). The ions can be clearly divided into two different groups: (i) heavy ions, where the first solvent shell follows the ion, and (ii) light ions, where only a partial following of the first solvent shell takes place. Note, however, that the electron impurity is different in this respect as its added mass arises solely from Eq. (6). The behavior of halogen anions is also shown in Fig. 7, where it can be seen that they do not appear to belong to either category. When this fact is combined (see also Table V) with the static liquid density profile calculations, it appears highly unlikely that the experimental halogen ion mobility data are due to these ions but rather to some other negatively charged species. Their mobilities should be approximately twice as high as reported in the literature to correlate with the positive ion data (see the arrows in Fig. 7).[1] Furthermore, the mobilities were reported to be below that of the solvated electron, which has no bound central potential and thus should be the largest ionic object possible in the liquid (excluding the possible multielectron bubbles with a large number of electrons and some molecular ions). In contrast, halogen atoms have high electron affinities (∼3 eV), which causes the electron spatial extent to be much smaller than for the solvated electron, and they also have a significantly smaller spatial zero-point spread inside the cavity than the electron due to their larger masses. It therefore appears that the laser ablation method,[1] which was used to produce the ions above the superfluid, forms other negatively charged species that are then observed in the subsequent ion drift experiment. While at first it would be tempting to assign these just to solvated electrons, there appears to be a small variation of the observed ion mobility depending on the atomic precursor,[1] and therefore these ions may be more complex than just electrons. The predicted halogen ion mobilities based on the present calculations are in the range of 0.8–1.0 cm^2 V^{-1} s^{-1} at 1.3 K, and they should have the following order: $\mu(I^-) > \mu(Br^-) > \mu(Cl^-) > \mu(F^-)$.

Future work based on the developed method will concentrate on the study of critical phenomena in superfluid helium (e.g., roton and vortex emission) when ions are accelerated to higher velocities,[2] and it will elucidate the origin of the well-known exotic ion signals in a similar time-of-flight measurement, where it will be essential to understand the relationship between mobilities and bubble sizes.[3]

ACKNOWLEDGMENTS

Financial support from the National Science Foundation, Grants No. CHE-0949057 and No. DMR-1205734, and the Interdisciplinary Research Institute for the Sciences (IRIS) is gratefully acknowledged. S.L.F. and J.E. acknowledge the computational resources provided by the Extreme Science and Engineering Discovery Environment (XSEDE) program, Grants No. CHE-100150 and No. CHE-110056, respectively.

*Jussi.Eloranta@csun.edu

[1] A. Kasimov, C. Zühlke, K. Jungmann, and G. zu Putlitz, Physica B **329-333**, 352 (2003).
[2] W. I. Glaberson and W. W. Johnson, J. Low Temp. Phys. **20**, 313 (1975).
[3] G. G. Ihas, Ph.D. thesis, University of Michigan, Ann Arbor, MI, 1971.
[4] G. G. Ihas and J. T. M. Sanders, Phys. Lett. A **31**, 502 (1970).
[5] J. Eloranta and V. A. Apkarian, J. Chem. Phys. **117**, 10139 (2002).
[6] D. Mateo, M. Pi, and M. Barranco, Phys. Rev. B **81**, 174510 (2010).

[7]K. W. Schwarz, Phys. Rev. A **6**, 1558 (1972).
[8]M. Foerste, H. Guenther, O. Riediger, J. Wiebe, and G. zu Putlitz, Z. Phys. B **104**, 317 (1997).
[9]K. R. Atkins, Phys. Rev. **116**, 1339 (1959).
[10]A. F. Borghesani, *Ions and Electrons in Liquid Helium* (Oxford Science, Oxford, 2007).
[11]A. G. Khrapak and W. F. Schidt, Int. J. Mass. Spectrom. **277**, 236 (2008).
[12]A. G. Khrapak and W. F. Schidt, Low Temp. Phys. **37**, 387 (2011).
[13]A. G. Khrapak, JETP Lett. **86**, 252 (2007).
[14]S. Paolini, F. Ancilotto, and F. Toigo, J. Chem. Phys. **126**, 126 (2007).
[15]M. Buzzacchi, D. E. Galli, and L. Reatto, Phys. Rev. B **64**, 094512 (2001).
[16]D. E. Galli, M. Buzzacchi, and L. Reatto, J. Chem. Phys. **115**, 10239 (2001).
[17]M. Rossi, M. Verona, D. E. Galli, and L. Reatto, Phys. Rev. B **69**, 212510 (2004).
[18]D. E. Galli, D. M. Ceperley, and L. Reatto, J. Phys. Chem. A **115**, 7300 (2011).
[19]R. M. Bowley, J. Phys. C **4**, 1645 (1971).
[20]R. Barrera and G. Baym, Phys. Rev. A **6**, 1558 (1972).
[21]F. Aitken, Z.-L. Li, N. Bonifaci, A. Denat, and K. von Haeften, Phys. Chem. Chem. Phys. **13**, 719 (2011).
[22]F. Aitken, N. Bonifaci, A. Denat, and K. von Haeften, J. Low Temp. Phys. **162**, 702 (2011).
[23]F. Dalfovo, A. Lastri, L. Pricaupenko, S. Stringari, and J. Treiner, Phys. Rev. B **52**, 1193 (1995).
[24]L. Lehtovaara, T. Kiljunen, and J. Eloranta, J. Comp. Phys. **194**, 78 (2004).
[25]L. Lehtovaara, J. Toivanen, and J. Eloranta, J. Comp. Phys. **221**, 148 (2007).
[26]F. Ancilotto, M. Barranco, F. Caupin, R. Mayol, and M. Pi, Phys. Rev. B **72**, 214522 (2005).
[27]F. Ancilotto, M. Pi, R. Mayol, M. Barranco, and K. K. Lehmann, J. Phys. Chem. A **111**, 12695 (2007).
[28]J. Eloranta, Phys. Rev. B **77**, 134301 (2008).
[29]L. Lehtovaara and J. Eloranta, *3-D Implementation of the Orsay-Trento Helium Density Functional*, http://libdft.sourceforge.net/.
[30]L. Lehtovaara and J. Eloranta, *Parallel Library for Processing Cartesian Grids*, http://libgrid.sourceforge.net/.
[31]L. Verlet, Phys. Rev. **159**, 98 (1967).
[32]H. J. Maris, J. Low Temp. Phys. **120**, 173 (2000).
[33]J. Wilks, *The Properties of Liquid and Solid Helium* (Clarendon, Oxford, 1967).
[34]J. Eloranta, N. Schwentner, and V. A. Apkarian, J. Chem. Phys. **116**, 4039 (2002).
[35]P. J. Knowles, C. Hampel, and H.-J. Werner, J. Chem. Phys. **99**, 5219 (1993).
[36]H.-J. Werner, P. J. Knowles, F. R. Manby, M. Schütz, P. Celani, G. Knizia, T. Korona, R. Lindh, A. Mitrushenkov, G. Rauhut *et al.*, MOLPRO, *Version 2010.1, A Package of ab initio Programs* (2010), http://www.molpro.net.
[37]J. Eloranta and V. A. Apkarian, J. Chem. Phys. **115**, 752 (2001).
[38]J. Ahokas, T. Kiljunen, J. Eloranta, and H. Kunttu, J. Chem. Phys. **112**, 2420 (2000).
[39]F. Boys and F. Bernardi, Mol. Phys. **19**, 553 (1970).
[40]D. E. Woon and T. H. Dunning, J. Chem. Phys. **103**, 4572 (1995).
[41]T. H. Dunning, J. Chem. Phys. **90**, 1007 (1989).
[42]D. E. Woon and T. H. Dunning, J. Chem. Phys. **98**, 1358 (1993).
[43]A. K. Wilson, D. E. Woon, K. A. Peterson, and T. H. Dunning, J. Chem. Phys. **110**, 7667 (1999).
[44]B. P. Prascher, D. E. Woon, K. A. Peterson, J. T. H. Dunning, and A. K. Wilson, Theor. Chem. Acc. **128**, 69 (2011).
[45]D. Rappoport and F. Furche, J. Chem. Phys. **133**, 134105 (2010).
[46]R. Ahlrichs, H. J. Böhm, S. Brode, K. T. Tang, and J. P. Toennies, J. Chem. Phys. **88**, 6290 (1988).
[47]A. D. Koutselos, E. A. Mason, and L. A. Viehland, J. Chem. Phys. **93**, 7125 (1990).
[48]I. Roeggen, H. R. Skullerud, and M. T. Elford, J. Phys. B **29**, 1913 (1996).
[49]R. Moszynski, B. Jeziorski, G. H. F. Diercksen, and L. A. Viehland, J. Chem. Phys. **101**, 4697 (1994).
[50]E. Czuchaj, F. Rebentrost, H. Stoll, and H. Preuss, Chem. Phys. **207**, 51 (1996).
[51]A. Giusti-Suzor and E. Roueff, J. Phys. B **8**, 2708 (1975).
[52]A. M. Gardner, C. D. Withers, J. B. Raneek, T. G. Wright, L. A. Viehland, and W. H. Breckenridge, J. Phys. Chem. A **114**, 7631 (2010).
[53]A. W. K. Leung and W. H. Breckenridge, J. Chem. Phys. **111**, 9197 (1999).
[54]G. Frenking, W. Koch, D. Cremer, J. Gauss, and J. F. Liebman, J. Phys. Chem. **93**, 3397 (1989).
[55]E. Coccia, F. Marinetti, E. Bodo, and F. A. Gianturco, Chem. Phys. Phys. Chem. **9**, 1323 (2008).
[56]B. J. Gray, T. G. Wright, E. L. Wood, and L. A. Viehland, Phys. Chem. Chem. Phys. **8**, 4752 (2006).
[57]E. F. Archibong, C. H. Hu, and A. J. Thakkar, J. Chem. Phys. **109**, 3072 (1998).
[58]F. Y. Naumkin and F. R. W. McCourt, Chem. Phys. Lett. **292**, 63 (1998).
[59]K. K. Lehmann, Phys. Rev. Lett. **88**, 145301 (2002).